

Evolution of static to dynamic mechanical behavior in topological nonreciprocal robotic metamaterials

Zehuan Tang^a, Yuanwen Gao^{a,*}

^aKey Laboratory of Mechanics on Environment and Disaster in Western China, The Ministry of Education of China, Lanzhou University, Lanzhou, Gansu 730000, PR China

ABSTRACT

Based on the Maxwell-Beatty reciprocity theorem, static non-reciprocity has been realized by using nonlinearity, but this non-reciprocity has strict restrictions on input amplitude and structure size(number of units). Here, we design a robotic metamaterial with two components of displacement and rotation, which uses active control to add external forces on the units to break reciprocity at the level of the interactions between the units. We show analytically and simulatively that breaking reciprocity at the level of the interactions directly leads to a strong asymmetric response of displacement in a static system, this displacement-specific characteristic not only has no restrictions on size, input amplitude, and suitable geometric asymmetry, but also can be transferred to rotation by coupling under large deformation. After the evolution from statics to dynamics, asymmetric transmission and unidirectional amplification of vector solitons are both implemented in this system. Our research uncovers the evolution of static non-reciprocity to dynamic non-reciprocity while building a bridge between non-reciprocity physics and soliton science.

Key words: Non-reciprocity; Asymmetric response; Unidirectional amplification; Solitons;

1. Introduction

Reciprocity is a fundamental property of linear, time-reversal invariant, and

spatial-reversal invariant physical systems, in which the excitation and response are symmetric [1]. Reciprocity can also sometimes be seen as a hindrance, for example in the case of reciprocity, there is no way to tune the response to different levels under excitation from different sides. Breaking this limitation of reciprocity is expected to achieve full control over static and dynamic responses. In the last few years, there has been a surge of interest in breaking reciprocity in mechanical systems[2-6], which achieve non-reciprocity primarily through two following schemes. One is to break the time-reversal symmetry of the system by adding active time-modulated components, which are generally used to achieve dynamic non-reciprocity. Typical examples are active metamaterials[7-10] and gyroscopic metamaterials[11, 12], which realize the propagation of non-reciprocal waves. The other is to break spatial symmetries of the passive structure through nonlinearity, which is usually used to achieve static non-reciprocity. For example, in topologically trivial ‘fishbone’ metamaterials[13-15], the structure has an asymmetrical response under different side excitation, while in topologically non-trivial rotating square metamaterials[13, 16], the response has greater asymmetry under different side excitation. This not only proves that breaking spatial symmetry is a powerful means to achieve non-reciprocity, but also shows that structures with topological properties can achieve more significant non-reciprocity.

In conventional topological band theory, the principle of bulk-edge correspondence (BEC) directly relates the number of topological boundary modes to the topological invariants under periodic boundary conditions (PBC)[17, 18]. The combination of non-reciprocity and topological band theory extends conventional band topology, such as zero modes based on the geometric asymmetry[13] and gain/loss induced nontrivial topological phases[19-21], and reveals a new class of topological phases characterized by non-Bloch winding numbers[22-24]. Perhaps the phenomenon of most interest in this novel spectral topology is the non-Hermitic skin effect (NHSE), where eigenstates in a system with broken reciprocity decay exponentially from the system boundary, and all eigenstates are localized at the boundary of the finite-sized system[25]. In the field of metamaterials, NHSE is generally achieved by adding active modulated components, which inevitably

inject/extract energy into a closed system.

Recently, the idea of combining active metamaterials and robotics has been proposed, and robotic metamaterials that combine local sensing, computation, communication, and actuation functions have been designed[26], which can achieve more extreme performance and different combinations of performance[27]. The concept of robotic metamaterials stems from the "programmability problem"[28], whereby shape-changing robots designed in this way are often complex because the microprocessors inside each robot need to communicate with all the other microprocessors in the lattice. Since then, the design idea of the common command instruction has greatly simplified the design of robot metamaterials, when the material is loaded externally, each robot only needs to respond to the information passed to them by the neighboring unit according to the common instruction[29]. Based on this, we design a robotic mechanical metamaterial that uses a distributed active control to break reciprocity at the level of the interactions between units, which results in the spatial symmetry of the structure being broken. This robotic metamaterial compares to conventional active or passive metamaterials, in addition to having a unique function that allows standing waves to achieve unidirectional amplification at all frequencies[26], our study shows that it also has a range of more extreme properties in static behavior, such as the realized non-reciprocity is not limited by structural size, the magnitude of input amplitude and geometric asymmetry. In particular, in the current study of vector soliton regulation, both active and passive metamaterials basically change the bond parameters, either directly or indirectly[30, 31]. Therefore, besides using the amplitude gap of vector solitons to realize the unidirectional transmission[32], usually unable to achieve asymmetric transmission under excitation from different sides. However, the robotic metamaterial we designed is based on the perspective of energy injection/extraction into the system, so it can realize both unidirectional amplification and asymmetric transmission of vector solitons.

2. Non-reciprocal robotic metamaterials

The one-dimensional chain consists of a rigid cross-unit with mass m , rotational inertia J , and arm length l , and the crosses are connected by shims of length l_h . Each cross is equipped with a local control device, which applies a force related to the displacement of neighboring units in the cross, the non-reciprocity at the level of the interactions can be achieved when the force and displacement satisfy the appropriate relationship. The specific design scheme as follows: the sensor of the local control device on the $(n-1)$ -th cross and $(n+1)$ -th cross needs to collect their displacement signal $u_{n\pm 1}$, and finally transmit the collected displacement signal to the control device on the n -th cross, the control device adds a rightward force $F_n = k_n(u_{n-1} - u_{n+1})$ to the n -th cross, as shown in Fig. 1(a). For mathematical modeling of the system, F_n is modeled as the resultant force of the leftward force $F_{n,n-1}$ and the rightward force $F_{n,n+1}$, as shown in Fig. 1(b), which satisfy the relation $F_{n,n+1} - F_{n,n-1} = F_n$. It is worth mentioning that in order to explain the problem more easily in different cases, $F_{n,n-1}$ and $F_{n,n+1}$ can be modeled in any form if the conditions of the resultant relation are satisfied. For example, under the PBC, $F_{n,n-1} = k_n(u_n - u_{n-1})$ and $F_{n,n+1} = -k_n(u_{n+1} - u_n)$ are selected for the modeling of the equivalent system, a pair of actuation forces between neighboring units in Fig. 1 (b) can be equivalent to the interaction force generated by the spring connection. The spring will have a special property — the force at both ends of the spring is not equal — namely, when the n -th node acts on the $(n+1)$ -th node, the stiffness is k_n , while when the $(n+1)$ -th node acts on the n -th node, the opposite negative stiffness $-k_n$ is presented, the modeling of the equivalent system is shown in Fig. 1(c). In this equivalent system, reciprocity at the level of the interactions is violated, which provides conditions for the realization of non-reciprocal effects. In addition, as shown in Fig. 1(c), shims connecting the crosses are

modeled as a combination of tension, torsion, and shear springs with stiffness k_l , k_θ , and k_s , and the tension stiffness k_l and shear stiffness k_s are much greater than the torsion stiffness k_θ .

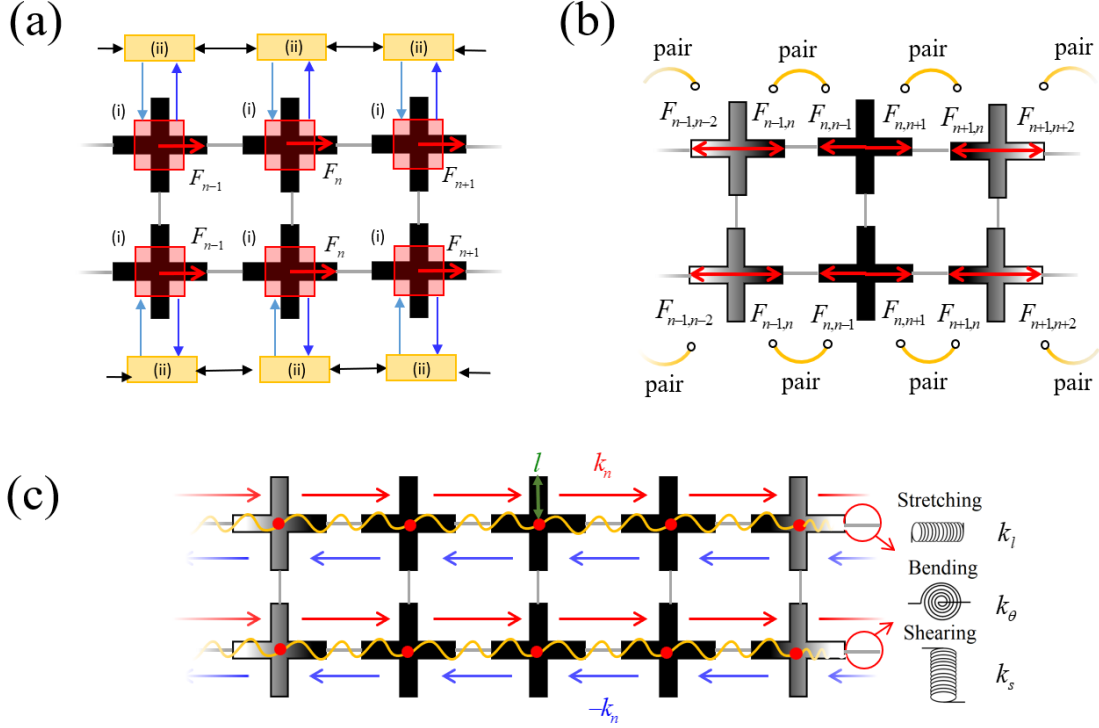


Fig. 1. (a) Design of nonreciprocal robotic metamaterials, (i) is the sensor, (ii) is the actuation device, and the arrow indicates the loop. (b) Modeling diagram of the system. (c) Modeling diagram of the equivalent system under PBC.

3. Static non-reciprocity

3.1. Pure displacement framework

First, we discussed the case where the actuation force on the left and right ends is also at the center of mass, namely, the structure is in the pure displacement situation without rotation angle. The structure can be regarded as a one-dimensional mass-spring system, and the control equation of displacement is as follows:

$$m \frac{\partial^2 u_n}{\partial t^2} = k_n (u_{n-1} - u_{n+1}) + k_l (u_{n+1} + u_{n-1} - 2u_n). \quad (1)$$

In general, the band theory is used to analyze the system under PBC, and the winding

number of a closed loop formed by branches can effectively represent the number of boundary modes of the finite structure. However, due to the possible skin effect in non-reciprocity systems, the traditional principle of BEC may fail in systems where reciprocity is broken[25, 33]. In our non-reciprocal system, the winding number under PBC produces singular results that cannot be used to characterize topological properties (see Appendix A for details). Discussion of the specific topological properties of non-reciprocal systems will need to be conducted under open boundary conditions(OBC). The modeling diagram of the finite structure of the N' ($N' = N + 1$) nodes is shown in Fig. 2(a). Under the condition of satisfying the overall horizontal external force balance, namely:

$$F_{0,1} + \sum_1^{N-1} (F_{n,n+1} - F_{n,n-1}) - F_{N-1,N} = 0,$$

the general formulas of actuation force can be written as $F_{n,n-1} = -k_n(u_n + u_{n-1})$ and $F_{n,n+1} = -k_n(u_{n+1} + u_n)$, so the controlling equation of the finite structure is:

$$-m\omega^2 \mathbf{U} = \mathbf{D}_{N' \times N'} \mathbf{U}, \quad (2)$$

where, $\mathbf{D}_{N' \times N'}$ is the total stiffness matrix of the finite structure (see Appendix A for specific form). The result of solving the 30 nodes is shown in Fig. 2(b), an isolated band appears at the zero frequency in the band gap, as shown in the red solid line of the figure. For the analysis of this isolated band, Eq. (2) degenerates to $\mathbf{D}_{N' \times N'} \mathbf{U} = 0$ at zero frequency, and $\{u_n\}$ is a geometric series, namely:

$$u_n = u_0 [g(k_n)]^n, \quad (3)$$

where, $g(k_n) = c_1 / c_2 = (k_l + k_n) / (k_l - k_n)$ is the local factor of the mode.

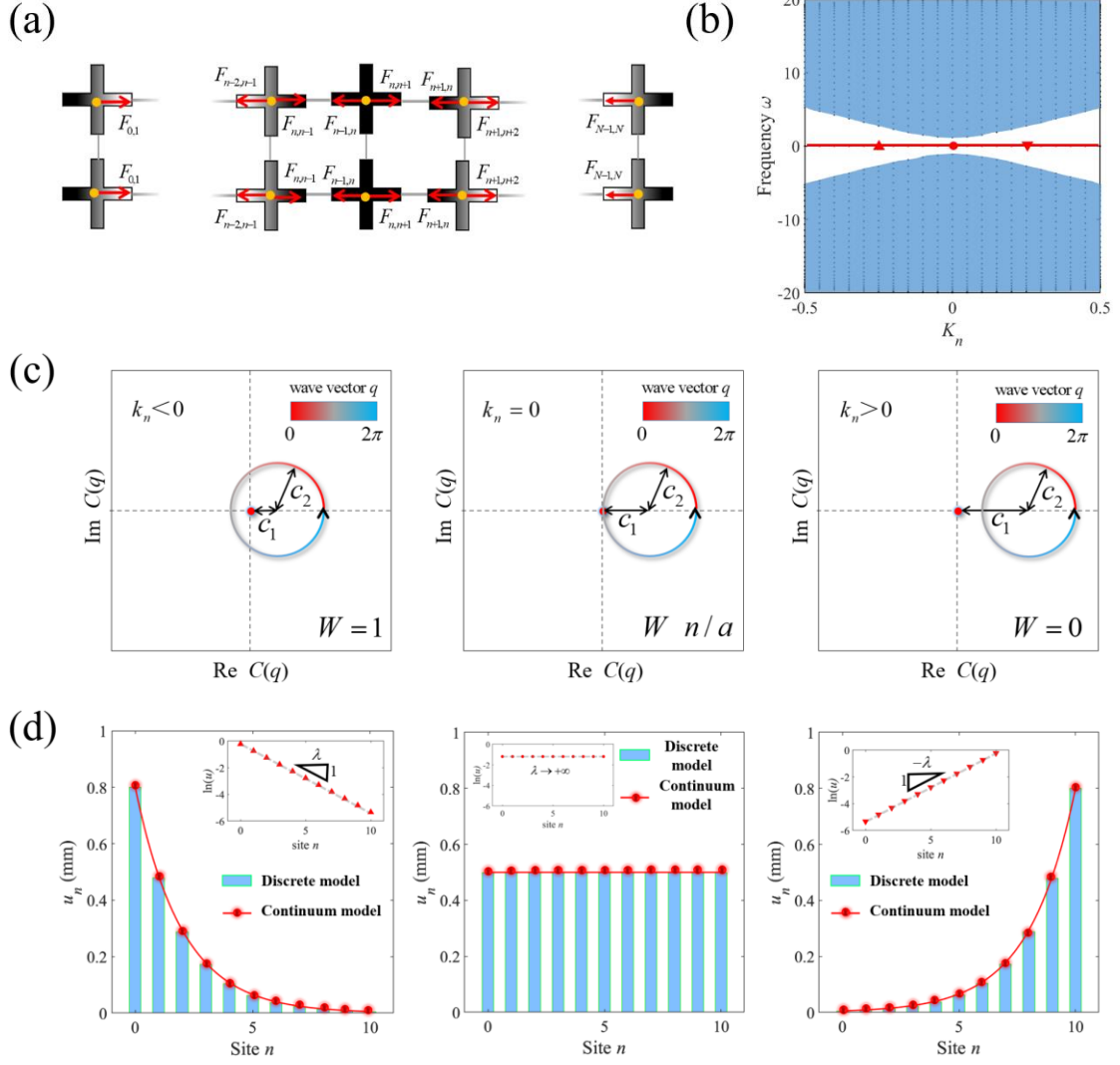


Fig. 2. (a) Schematic diagram of the OBC. (b) Spectra of the structures at the OBC. (c) The topological invariant changes with k_n . (d) The distribution diagram of the modes of the finite structure ($N' = 11$), inset is the distribution diagram after linearizing u_n .

Further analysis of the above phenomenon, in the deformation process, the work done by the n -th pair of actuation forces ($F_{n,n+1}$ and $F_{n+1,n}$) is:

$$E_{n,n+1} = \int F_{n,n+1} du_n - \int F_{n+1,n} du_{n+1} = k_l (g-1)^2 u_n^2 / 2,$$

the strain energy required for the shim deformation between the n -th and $(n+1)$ -th node is:

$$U_{n,n+1} = k_l (u_{n+1} - u_n)^2 / 2 = k_l (g-1)^2 u_n^2 / 2,$$

namely, $E_{n,n+1} - U_{n,n+1} = 0$. This shows that the work injected by the actuation force

between units to the chain is exactly all used for the corresponding shim between units. If the control device and the one-dimensional chain are equivalent to a system, the system supports a mode that is similar to the zero-energy modes, this corresponds well to the previously reported topological zero-energy modes[34, 35]. According to the above energy equality relationship, $F_{n,n+1}$ and $F_{n+1,n}$ should be equal to the reaction force generated by the tensioned shim, namely, $F_{n,n+1} = F_{n+1,n} = -k_l(u_{n+1} - u_n)$, for a finite structure of N' nodes, write the above formula in matrix form:

$$\mathbf{C}_{(N'-1) \times N'} \mathbf{U} = 0, \quad (4)$$

where, $\mathbf{C}_{(N'-1) \times N'}$ is the compatibility matrix (see Appendix A for the specific form).

The Fourier transform of the compatibility matrix \mathbf{C} yields $C(q) = c_1 - c_2 e^{iq}$, when the wave vector q changes from 0 to 2π , $C(q)$ forms a circle in the complex plane.

The circle of the complex plane has an obvious spectral winding number, which is defined as $W = (2\pi i)^{-1} \int_0^{2\pi} 1/C(q) dC(q)$. Fig. 2(c) shows the change of topological invariants with k_n .

When $k_n < 0 (g < 1)$, the circle goes once around the origin, and the topological invariant $W=1$, in the case of $N \rightarrow +\infty$, u_n is an admissible eigenstate near the boundary $n=N$;

When $k_n = 0 (g = 1)$, the circle passes through the origin, at this point, W is singular, with a topological transition in the one-dimensional chain. When

$k_n > 0 (g > 1)$, the topological invariant W changes to 0, u_n is not an admissible eigenstate near the boundary $n=N$. Fig. 2(d) shows the distribution of displacements corresponding to zero frequency for a finite structure with 11 nodes, the insets is the linearized displacement distribution diagram. It can be seen that when $k_n \neq 0$, the

modes are exponentially distributed, and the decay length a is defined as the length required to decay a unit in the logarithmic coordinate, namely, $\lambda = 1 / \ln(u_n / u_{n+1})$, and the decay length reflects the decay speed of the boundary mode. When $W=1$, the

decay length is positive, and the mode localization is on the left. When W is singular,

the decay length is negative, and the mode localization is on the right.

the decay length tends to positive infinity, and the modes are delocalized, which appear as body modes. When $W=0$, the decay length is negative, displacement increases exponentially with the increase of the node number, and the mode locality is on the right. With the k_n symbol unchanged, the modes only localize on a specific side of the chain to provide conditions for the implementation of static non-reciprocity.

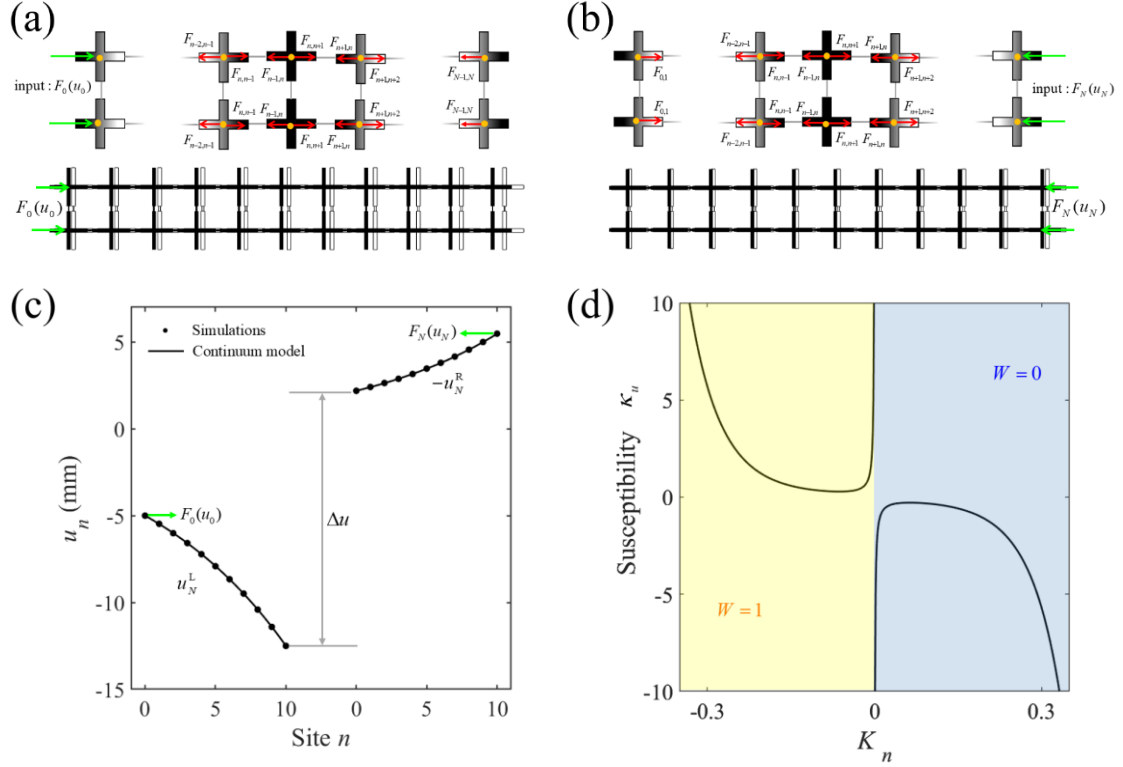


Fig. 3. (a), (b) the simulation results of the left and right excitation at $k_n / k_l = 0.05$, respectively. The top figure is the excitation schematic diagram, the lower figure is the simulation result, the hollow cross not filled with the color is the initial state, and the cross filled by the color is the deformation after the excitation. When the left side is excited, the displacement increases from the incentive side to the right side. When the right side is excited, the displacement tends to decay from the excitation side to the left side. (c) The static non-reciprocity of the displacement. (d) The non-reciprocal susceptibility κ_u diverges at $K_n = 0$, where $K_n = k_n / k_l$.

In the simulation software COMSOL creates a chain of N' nodes, without general we choose $N' = 11$, and use the built-in probe function to monitor the

displacement of u_n , monitor displacement u_n to add actuation force on each node, the way of actuation force described in Fig. 2(a), but the difference is the start nod (the first node for the left incentive and the last node for the right excitation) without actuation force. Firstly, the one-dimensional chain is excited on the left, and a rightward force $F_0(u_0)$ is input at the first node to deform the chain. The results show that the displacements of each node tend to increase with the increase of node number, as shown in Fig. 3(a). Input a leftward force $F_N(u_N)$ to excite the one-dimensional chain, and the displacement decays from the excitation side to the left side, as shown in Fig. 3(b). In the case of $F_0 = F_N$, there is a huge difference between u_N^L under left excitation and $-u_0^R$ under right excitation, which indicates that the displacement response has obvious static non-reciprocity, as shown in Fig. 3(c). The displacement difference of left and right excitation increases with the increase of excitation amplitude and structure size, and the relationship between them is as follows (see Appendix A for details) : $\Delta u = \kappa_u(k_n)F_0$, Δu and F_0 present a primary dependence relationship, where κ_u is non-reciprocal susceptibility, and it is specifically expressed as follows:

$$\kappa_u(k_n) = -\frac{g^N + g^{1-N}}{k_l(g-1)}. \quad (5)$$

The variation of κ_u concerning to k_n is shown in Fig. 3(d), it can be seen that when k_n changes from negative to positive, κ_u appears infinite discontinuity at $k_n = 0$, which is because W jumps from 1 to 0 with the change of k_n , the underlying mechanism of one-dimensional chain changes from displacement localization on the left to localization on the right after delocalization, and the transformation of the displacement distribution from the boundary mode to the body mode($g \rightarrow 1$) leads to the divergence of κ_u .

3.2. Geometric linear framework

The excitation mode of the starting node in section 3.1 is transformed into the force deviating from the center of mass, as shown in the excitation form in Fig. 4(a). In this case, the one-dimensional chain not only has displacement deformation, but also has rotation deformation. First, consider the case where the eccentricity distance is very small, namely, the angle is very small, the deformation of the structure can be approximated as a linear small deformation. Therefore, geometric nonlinearity is not considered in the simulation, and the simulation results are shown in Fig. 4(a). Under the left and right excitation respectively, the displacement distribution is consistent with Fig. 3(a), which shows obvious non-reciprocity, and the response under left excitation is increasing (top figure), response under right excitation is decaying (lower figure). However, no matter the left excitation or the right excitation, the angle fields all appear to decay inward, and the angle distribution remains symmetric when $F_0 = F_N$, presenting reciprocity, as shown in Fig. 4(c).

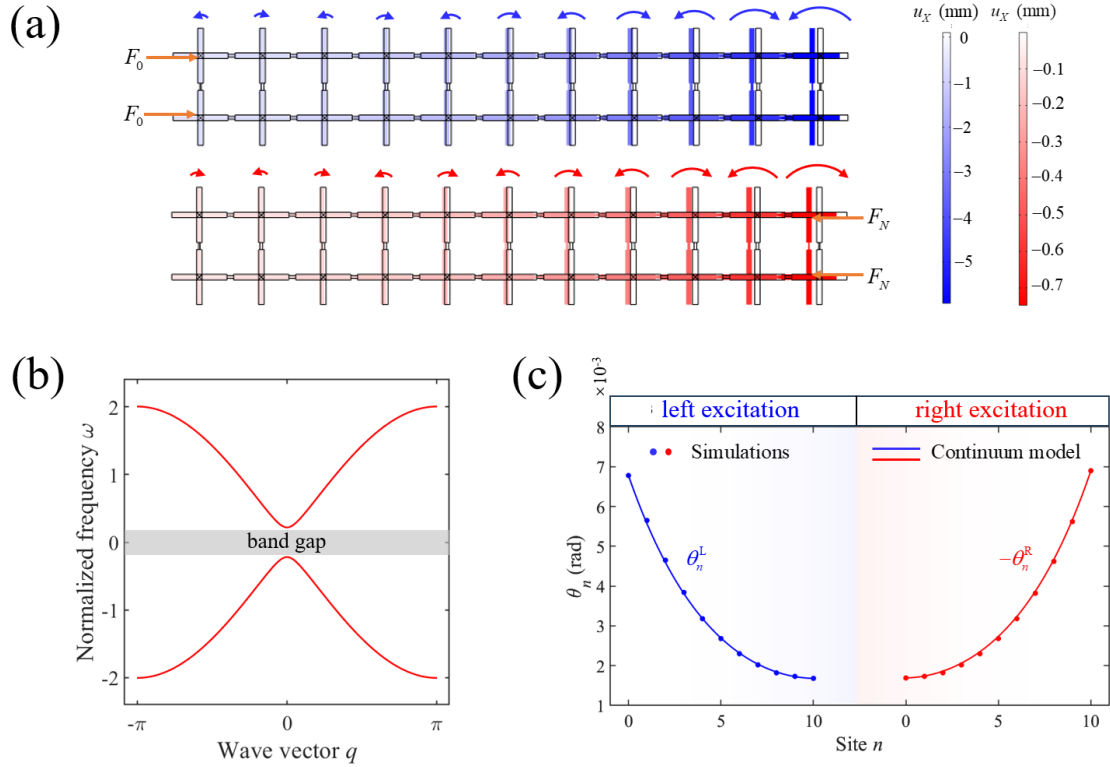


Fig. 4. (a) The top and lower figures are the simulation results of the left and right eccentric excitation, respectively, where the scaling factors of the top and lower figures are 1 and 10, respectively. The depth

of the filling color of the cross represents the magnitude of the x component of its displacement field, and the arrow and arc length of the arc above the cross represent the direction and magnitude of the angle respectively. (b) The dispersion diagram of the angle. (c) The angle is reciprocal at small deformation, and the blue line (left excitation) and the red line (right excitation) are symmetrical in the figure.

In order to better analyze and understand the above phenomena, a theoretical model of linear small deformation is established. In the modeling of the geometric linear framework, the angle θ_n is assumed to be infinitesimal, and the displacement u_n and angle θ_n are both approximated as a first-order expansion concerning the excitation F_0 , namely:

$$u_{n+1} - u_n = -(1/k_l)F_{n+1,n}. \quad (6)$$

In Eq. (6), the influence of angle is truncated as higher-order infinitesimal, and Eq.(6) indicates that the distribution of displacement deformation will conform to the distribution of pure displacement in section 3.1.

For angle deformation, the governing equation is expressed as:

$$0 = -k_\theta(\theta_{n+1} + \theta_{n-1} + 4\theta_n) + k_s l^2(\theta_{n+1} + \theta_{n-1} - 2\theta_n). \quad (7)$$

When the band theory is used to analyze the angle (see Appendix B for details), because the torsional stiffness k_θ of the shim is non-zero, this results in $\omega(0)$ never being zero, so that the zero frequency is always in the band gap, as shown in Fig. 4(b). This indicates that the angle field corresponds to a no propagating mode at zero frequency, and no matter from which side the excitation is carried out, the angle distribution will appear to decay inward. The angle control equation Eq. (7) in the continuum limit form is:

$$\frac{d^2\theta}{dX^2} - \left(\frac{1}{\lambda_\theta^*}\right)^2\theta = 0, \quad (8)$$

where $\lambda_\theta^* = \sqrt{(k_s l^2 - k_\theta)/(6k_\theta)}$, it is the characteristic decay length of the angle distribution. Eq. (8) has the spatial symmetry of $X \rightarrow -X$, $\theta \rightarrow -\theta$, which confirms

that the angle is reciprocal in the case of linear small deformation. The solution of Eq. (8) consists of a linear combination of $\exp(X / \lambda_\theta^*)$ and $\exp(-X / \lambda_\theta^*)$, namely :

$$\theta = c_1 e^{X / \lambda_\theta^*} + c_2 e^{-X / \lambda_\theta^*}. \quad (9)$$

The results of Eq. (9) are shown in the solid line in Figure 4(c), where the solution for the left excitation (blue line) and the solution for the right excitation (red line) are symmetrically distributed.

3.3. Geometric nonlinear frame

When the eccentric distance of the force is further increased, the one-dimensional chain enters the large deformation of the angle, and the linear small deformation hypothesis of the upper section is no longer applicable. First, the response of the one-dimensional chain with large deformation under left and right excitation is simulated in the simulation software. At this time, geometric nonlinearity is considered in the simulation, and in order to ensure that the angle deformation is within a reasonable range, the moment generated by the actuation force should be of the same order of magnitude as k_θ , so $k_n \ll k_l$ is satisfied in the simulation (our simulation model in this section, $k_n / k_l = 0.002$). The simulation results show a phenomenon completely different from that in section 3.2, namely, the angle field has an asymmetric response, and the comparison between left and right excitation is shown in Fig. 5(a). Next, we focus on the angle distribution under left excitation, and the simulation results show that the angle distribution is dependent on the end displacement deformation u_N . When u_N is positive, the angle distributions always decay from the left side (excitation side) to the right side, as shown in Fig. 5(b) and 5(c), and with the increase of u_N , the decay rate is faster, as shown in the inset in Fig. 5(c), the angle distribution curve corresponding to Fig. 5(b) (red line) is always below the angle distribution curve corresponding to Fig. 5(c) (black line). When u_N is negative, the angle distribution is still from the left side to the right side when $|u_N|$ is small, as

shown in Fig. 5(d); but when $|u_N|$ increases to a certain critical point, the angle distribution changes to increase from left side(excitation side) to right side, as shown in Fig. 5(e).

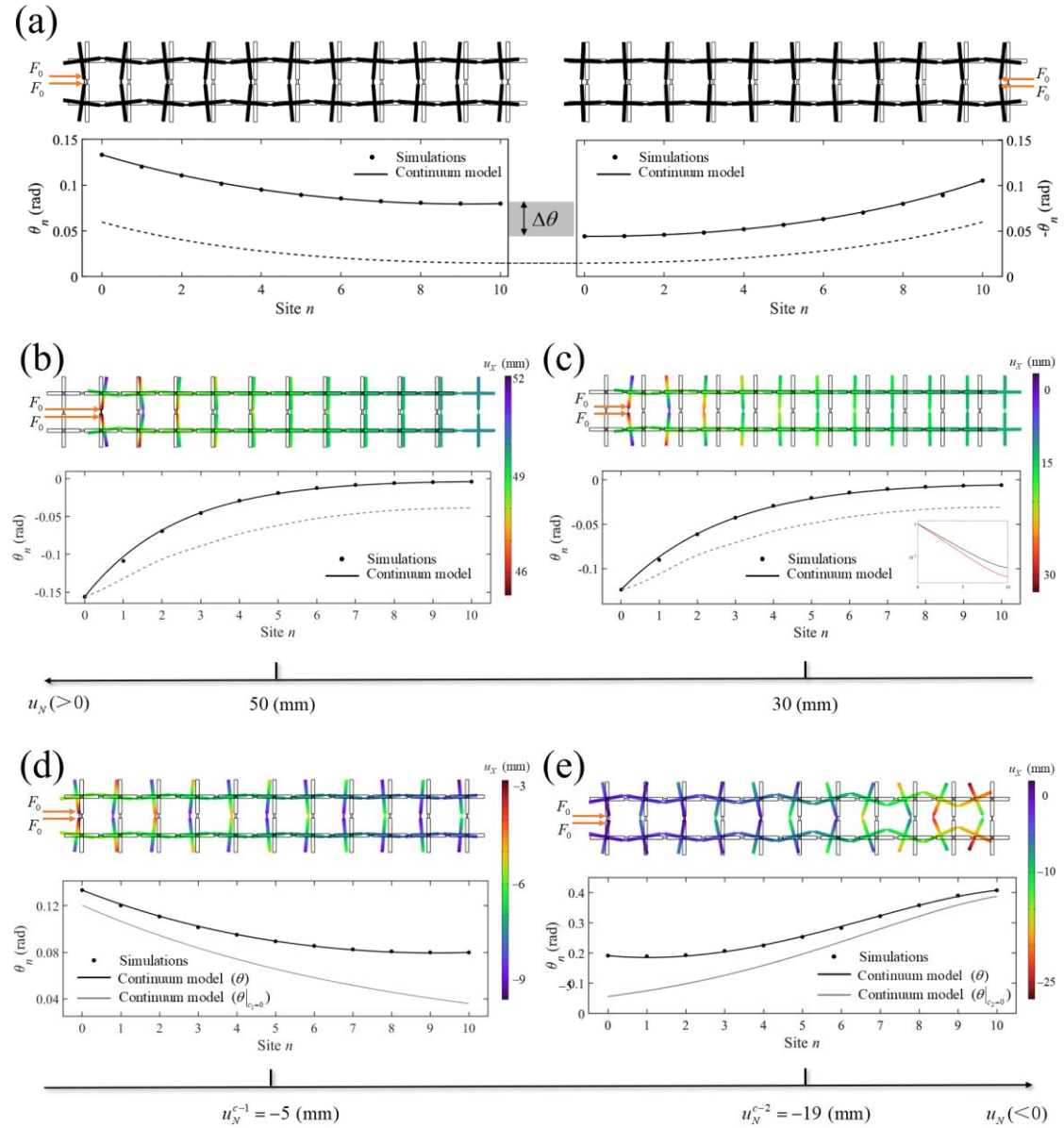


Fig. 5. (a) The top figure shows the simulation results of the left excitation and the right excitation, while the lower figure shows that the responses of the left excitation and the right excitation are asymmetrical, where the black solid dot is the simulation result and the black solid line is the result of the continuum model(Eq.(15)). The black dashed line is the result of the continuum model(Eq.(9)) without taking into account geometric nonlinearity, where the responses of the left and right excitation are symmetric. (b) and (c) are the resulting diagram corresponding to $u_N > 0$ under left excitation. (b) and (c) correspond

to the cases of $u_N = 50$ (mm) and $u_N = 30$ (mm) respectively, and their angle distribution decays from the left to the right, and their distribution curve (black line) is within the gray envelope, where the gray envelope(dashed line) corresponds to the angle distribution of $f_{n,n+1} = 0$. Inset is obtained by normalization of the angle distribution in Fig. 5(b) and Fig. 5(c). (d) and (e) are the resulting diagram corresponding to $u_N < 0$ under left excitation. (d) shows that the angle distribution decays from the left to the right when $u_N = u_N^{c-1}$, and as u_N decreases u_N^{c-2} , (e) shows that the angle distribution changes to increase from the left to the right. The solid gray lines in both figures are the distribution curves of the dominant deformation mode ($\theta|_{c_1=0}$ or $\theta|_{c_2=0}$).

To investigate the source of the non-reciprocal effect and the cause of decay and increase of two deformation modes, a theoretical model of the geometric nonlinear frame is established. Different from the modeling of geometric linear frames, in the modeling of the geometric nonlinear frame, the displacement difference of the centroid of the cross is modeled as:

$$u_{n+1} - u_n = -\frac{F_{n+1,n}}{k_l} - (l + \frac{l_h}{2})(2 - \cos \theta_n - \cos \theta_{n+1}), \quad (10)$$

which is composed of two parts: the deformation of the shim and the change of the horizontal projection generated by the rotation of the cross. According to Eq.(10), the governing equation of displacement is as follows:

$$\mathbf{C}_{(N-1) \times N} \mathbf{U} = -k_l l [a_0, \dots, a_n, \dots, a_{N-1}]^T, \quad (11)$$

where, $a_n = 2 - \cos \theta_n - \cos \theta_{n+1}$, $n \in [0, N-1]$. Let $a_N = 0$, the bit displacement solution can be written as:

$$u_n = c_0 g^n - (l + \frac{l_h}{2}) \sum_{i=n}^N a_i, \quad (12)$$

where $c_0 g^n$ is the general solution corresponding to the homogeneous form of Eq.(11)(namely, $\mathbf{CU} = 0$), c_0 is determined by the boundary conditions;

$(l + l_h / 2) \sum_{i=0}^{N-n} a_i$ is the particular solution corresponding to $U(N,1) = 0$, in the process of solving the particular solution, since $k_n \ll k_l$, two elements c_1 and c_2 in the compatibility matrix C are approximated by $c_1 = c_2 = k_l$, under this particular solution, $c_0 = u_N$. The governing equation for angle is as follows (see Appendix B for details):

$$\frac{d^2\theta}{dX^2} - \frac{2k_l l u_N g^X \ln g + 6k_\theta}{k_s l^2 - k_\theta} \theta = 0, \quad (13)$$

where, term g^X is generated due to the addition of actuation forces, and it is the addition of this term that makes the symmetry of $X \rightarrow -X, \theta \rightarrow -\theta$ in Eq.(13) no longer hold, which makes the angle deformation obtain non-reciprocal effect in nonlinear large deformation, which explains the asymmetric response in Fig. 5(a).

Eq. (13) is further simplified, as $\Delta = 2k_n / (k_l - k_n)$ in $g^X = [1 + \Delta]^X$ approaches 0, g^X in eq.(11) is simplified to $1 + \Delta X$, and a solvable differential equation is obtained:

$$\frac{d^2\theta}{dX^2} - (aX + b)\theta = 0, \quad (14)$$

where,

$$a = (2k_l l u_N \Delta \ln g) / (k_s l^2 - k_\theta),$$

$$b = (2k_l l u_N \ln g + 6k_\theta) / (k_s l^2 - k_\theta).$$

Eq. (14) corresponds to the stationary Schrodinger equation with linear potential energy, let $\zeta = (aX + b) / |a|^{2/3}$, the solution of Eq. (14) can be expressed as:

$$\theta = c_1 \text{Ai}(\zeta) + c_2 \text{Bi}(\zeta), \quad (15)$$

where $\text{Ai}(\zeta)$ and $\text{Bi}(\zeta)$ are Airy functions.

Next, two phenomena of decay and increase in left excitation are discussed. In the above modeling, the force on the shim between the n -th node and the $(n+1)$ -th node is written as:

$$f_{n,n+1} = k_l u_N (g^{n+1} - g^n). \quad (16)$$

When $u_N > 0$, all the forces on the internode shim are tensions. In this case, $f_{n,n+1}$ always exerts a moment on the cross to make the angle tend to 0, which makes the corresponding angle distribution of $u_N > 0$ fall within the envelope formed by the angle distribution of $f_{n,n+1} = 0$, as shown in Fig. 5(b) and Fig. 5(c), so in this case, the angle distribution can only decay from the left end to the right end. At the same time, with the increase of u_N , $f_{n,n+1}(u_N)$ also increases, which means an increase of the moment that forces the angle to 0, resulting in a faster decay rate, as shown in the inset in Fig. 5(c).

When $u_N < 0$, the force of each internode shim is all pressure, which meets the necessary condition that the angle increases from the left side to the right side — the force of the shim between the $(N-1)$ -th node and the N -th node must be pressure (see Appendix B for details). We focus on two critical cases, the first critical is $\theta(N-1) = \theta(N)$, and the $|u_N|$ is small at this time, which is denoting as u_N^{c-1} , and u_N^{c-1} is the critical point at which the angle distribution begins to have increasing intervals, as shown in the simulation results in Fig 5(d). The result of Eq.(15) is represented by the black solid line corresponding to the continuum model in Fig. 5(d), and the decay deformation mode $\theta|_{c_1=0}$ in Eq. (15) is represented by the gray solid line in Fig. 5(d), the trend of the gray solid line is almost consistent with that of the black solid line, indicating that the decay mode almost dominates the deformation at this time. The second critical is $\theta(0) = \theta(1)$, when $|u_N|$ is larger, and the $|u_N|$ at this time is denoting u_N^{c-2} , u_N^{c-2} corresponds to the critical where the angle can increase monotonously from the left side to the right side, as shown in the simulation results in Fig. 5(e). At this time, the increase of deformation mode $\theta|_{c_2=0}$ dominates the angle deformation, as shown in the results of the black solid line and the gray solid line in Fig. 5(e). In summary, with the decrease of u_N , the transition of angle distribution from attenuation to increase is the result of competition between decay and increase

deformation modes.

In this section, we not only demonstrate the feasibility of the scheme of transferring non-reciprocity from displacement to angle through coupling under large nonlinear deformation, but more importantly, we find that the amplitude of the angle can also increase with node number under appropriate conditions. In the following studies, we try to realize this phenomenon of increasing amplitude in dynamic systems. Inspired by the fact that actuation forces can input energy to the one-dimensional chain in the previous chapter, we attempt to apply this active regulatory force to a dynamic system with constant energy to achieve the phenomenon of increasing angle amplitude, the soliton system supported by the reverse rotating cross/square structure seems to be a good choice.

4. Dynamic non-reciprocity

In the study of dynamic behavior, we select a long chain with $N' = 201$ nodes, whose active regulatory force is applied in the same way as in Fig. 5(a), but unlike static loading, the dynamic excitation is shock excitation. The governing equations of dynamic modeling are as follows:

$$m \frac{\partial^2 u}{\partial t^2} - k_l \frac{\partial^2 u}{\partial X^2} - k_l (2l + l_h) \theta \frac{\partial \theta}{\partial X} = -2k_n \frac{\partial u}{\partial X}, \quad (17)$$

$$J \frac{\partial^2 \theta}{\partial t^2} + k_\theta (6\theta + \frac{\partial^2 \theta}{\partial X^2}) + 2k_l l [\frac{\partial u}{\partial X} + (l + \frac{l_h}{2}) \theta^2] \theta - k_s l^2 \frac{\partial^2 \theta}{\partial X^2} = 0. \quad (18)$$

The left side of the equation system corresponds to the governing equation of vector solitons, while the right side of the equation group has a perturbative term $-2k_n \partial_X u$. Numerical solutions of Eqs. (17) and (18) show that the amplitude of the pulse solitons increases with the increase of the node number when the left side is excited, as shown in Fig. 6(a). A schematic diagram of solitons in structural propagation is shown in Fig. 6(c). Then we also carry out shock excitation on the right side, and finally draw the spatiotemporal diagram of soliton propagation under left excitation and right excitation as Fig. 6(b). From the spatiotemporal diagram of the right

excitation, it can be seen that the amplitude of the soliton is decreasing. Different from the rule that the amplitude of the soliton is continuously increasing with a stable form under the left excitation, the amplitude of the soliton under the right excitation is not continuously decreasing to 0, but suddenly transforming into a strongly dispersive wave when it is below a specific amplitude. In addition, even before the solitary wave distortion, the solitary wave corresponding to the left and right excitation are asymmetrical, because the perturbative term breaks the spatial symmetry of the Eqs. (17) and (18).

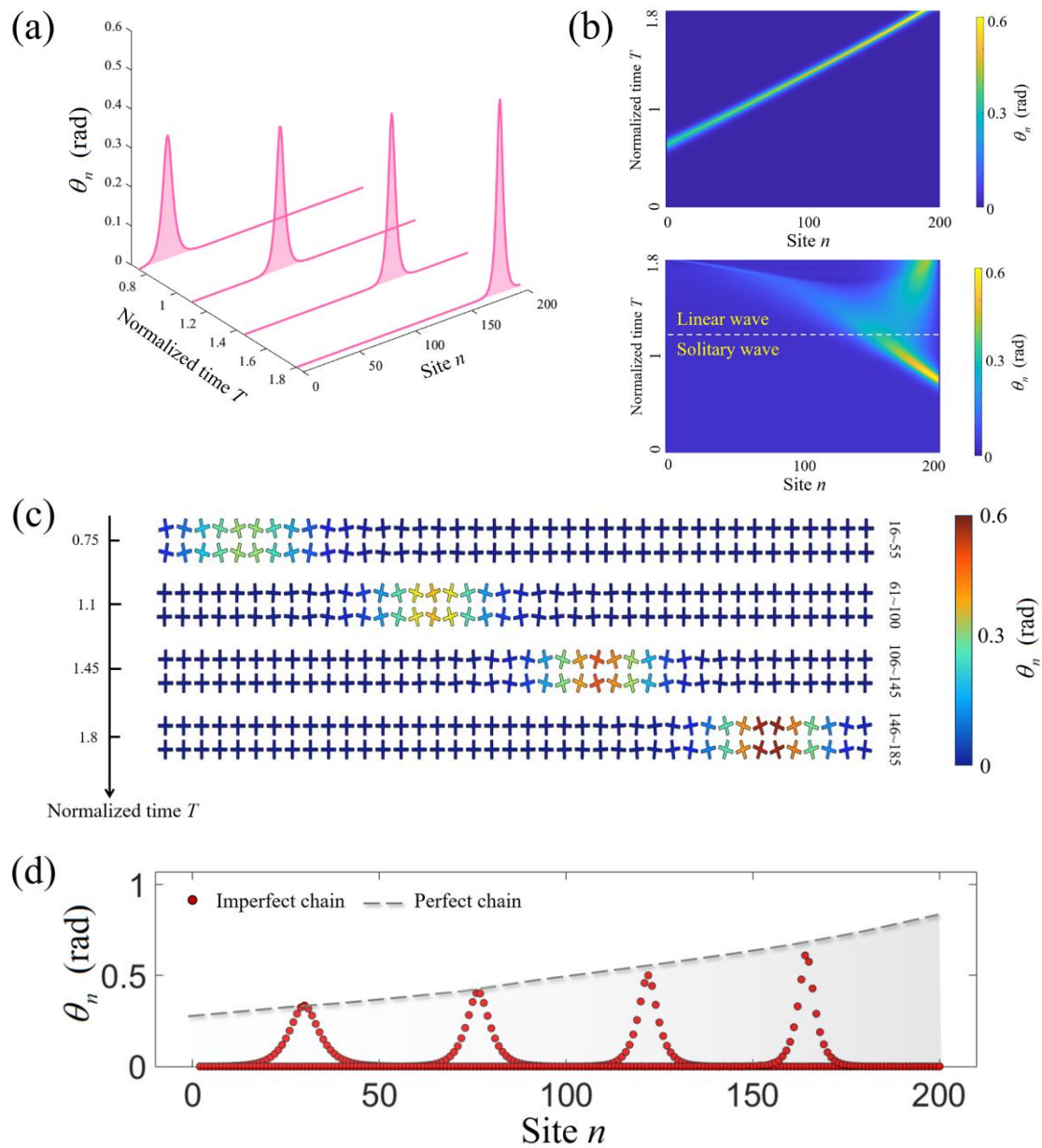


Fig. 6. (a) Under the left excitation, the amplitude of the soliton increases in the propagation process, and

$k_n / k_l = 6 \times 10^{-5}$. (b) Solitons maintain a stable form under the left excitation, and the amplitude increases during propagation (top figure). under the right excitation, the amplitude of soliton decreases during the propagation process, and maintains a stable form when the amplitude is greater than the amplitude gap. When the amplitude is reduced to the amplitude gap, the non-dispersive solitary wave transforms into a strongly dispersive linear wave (lower figure). (c) Deformation schematic diagram of numerical solution in structure. (d) A comparison diagram of the skin effects of defective structure(no active regulatory force at nodes 100-th to 110-th) and perfect structure.

As a soliton system with constant energy, this means that the energy change of the system will all come from the perturbation term, and the energy change of the soliton when it is transferred from the n -th node to the $(n+1)$ -th node is:

$$\Delta E_{n,n+1} = \int_{-\infty}^{+\infty} -2k_n l \frac{\partial u}{\partial X} \frac{\partial u}{\partial T} dT = 2ck_n l \int_{-\infty}^{+\infty} \left(\frac{\partial u}{\partial X} \right)^2 dT. \quad (19)$$

The result of Eq. (19) shows that the energy of solitons increases(decreases) when $c > 0 (c < 0)$. As shown in Fig. 6(a), the increase of soliton amplitude is accompanied by the decrease of width, which means that the amplitude and energy value may not meet the positive correlation. In Appendix C, we prove the positive correlation between the amplitude and energy value, namely, $dA / dE > 0$. Therefore, according to the modeling of Eq. (19), it can be obtained that when solitons propagate from left to right ($c > 0$), the active regulatory force injects energy to the chain, thereby increasing the amplitude of the solitons, while the right excitation ($c < 0$) is opposite. The soliton solution needs to satisfy a restriction condition that the soliton amplitude should be greater than the amplitude gap A_p^{gap} , the existence of the amplitude gap leads to the sudden distortion when the soliton amplitude is less than A_p^{gap} under the right excitation. At the same time, due to solitons having a permanent form, even if there are structural defects(some units have no active regulatory force), the solitons excited in our active system can realize unidirectional amplitude amplification with a stable form, as shown in Fig. 6(d).

5. Conclusion

To conclude, we propose a robotic metamaterial with two components of rotation and displacement, which has more extreme properties and different combinations of functions. Specifically, in the static behavior, the addition of active control breaks the spatial symmetry of the structure, which induces a topological nontrivial phase, thus achieving unidirectional amplification and asymmetric response in displacement. Then we demonstrate the feasibility of transferring non-reciprocal effects from displacement to angle under nonlinear large deformation, which lays a foundation for the study of dynamic behavior. In the dynamic behavior, amplitude unidirectional amplification and asymmetric transmission have been extended to soliton systems. This discovery links the skin effect and soliton science, and provides a new platform for the comprehensive regulation of solitary waves. We anticipate that these new characteristics will be expected to be used in crawling robots to overcome the effects of manufacturing errors and dissipation in the operating environment.

Declaration of Competing Interest

The authors declare that they have no known competing financial interests or personal relationships that could have appeared to influence the work reported in this paper.

Acknowledgments

This work was supported by the National Natural Science Foundation of China (Grant Nos. 12272154).

Reference

- [1] H. Nassar, B. Yousefzadeh, R. Fleury, M. Ruzzene, A. Alù, C. Daraio, A.N. Norris, G. Huang, M.R. Haberman, Nonreciprocity in acoustic and elastic materials, *Nature Reviews Materials* 5(9) (2020) 667-685.
- [2] L. Wang, J.A.I. Martínez, G. Ulliac, B. Wang, V. Laude, M. Kadic, Non-reciprocal and non-Newtonian mechanical metamaterials, *Nature Communications* 14(1) (2023) 4778.
- [3] H. Nassar, X.C. Xu, A.N. Norris, G.L. Huang, Modulated phononic crystals: Non-reciprocal wave propagation and Willis materials, *Journal of the Mechanics and Physics of Solids* 101 (2017) 10-29.
- [4] Y. Hadad, J.C. Soric, A. Alu, Breaking temporal symmetries for emission and absorption, *Proceedings of the National Academy of Sciences* 113(13) (2016) 3471-3475.
- [5] B.M. Goldsberry, S.P. Wallen, M.R. Haberman, Non-reciprocal wave propagation in mechanically-modulated continuous elastic metamaterials, *The Journal of the Acoustical Society of America* 146(1) (2019) 782-788.
- [6] G. Trainiti, M. Ruzzene, Non-reciprocal elastic wave propagation in spatiotemporal periodic structures, *New Journal of Physics* 18(8) (2016) 083047.
- [7] Y. Wang, B. Yousefzadeh, H. Chen, H. Nassar, G. Huang, C. Daraio, Observation of Nonreciprocal Wave Propagation in a Dynamic Phononic Lattice, *Physical Review Letters* 121(19) (2018) 194301.
- [8] Y. Chen, X. Li, H. Nassar, A.N. Norris, C. Daraio, G. Huang, Nonreciprocal Wave Propagation in a Continuum-Based Metamaterial with Space-Time Modulated Resonators, *Physical Review Applied* 11(6) (2019) 064052.
- [9] H. Nassar, H. Chen, A.N. Norris, G.L. Huang, Quantization of band tilting in modulated phononic crystals, *Physical Review B* 97(1) (2018) 014305.
- [10] H. Nassar, H. Chen, A.N. Norris, G.L. Huang, Non-reciprocal flexural wave propagation in a modulated metabeam, *Extreme Mechanics Letters* 15 (2017) 97-102.
- [11] L.M. Nash, D. Kleckner, A. Read, V. Vitelli, A.M. Turner, W.T.M. Irvine, Topological mechanics of gyroscopic metamaterials, *Proceedings of the National Academy of Sciences* 112(47) (2015) 14495-14500.

- [12] P. Wang, L. Lu, K. Bertoldi, Topological Phononic Crystals with One-Way Elastic Edge Waves, *Physical Review Letters* 115(10) (2015) 104302.
- [13] C. Coulais, D. Sounas, A. Alù, Static non-reciprocity in mechanical metamaterials, *Nature* 542(7642) (2017) 461-464.
- [14] M. Shaat, Nonreciprocal elasticity and the realization of static and dynamic nonreciprocity, *Scientific Reports* 10(1) (2020) 21676.
- [15] M. Shaat, M.A. Moubarez, M.O. Khan, M.A. Khan, A. Alzo'ubi, Metamaterials with Giant and Tailorable Nonreciprocal Elastic Moduli, *Physical Review Applied* 14(1) (2020) 014005.
- [16] C. Coulais, C. Kettenis, M. van Hecke, A characteristic length scale causes anomalous size effects and boundary programmability in mechanical metamaterials, *Nature Physics* 14(1) (2018) 40-44.
- [17] H. Chen, H. Nassar, G.L. Huang, A study of topological effects in 1D and 2D mechanical lattices, *Journal of the Mechanics and Physics of Solids* 117 (2018) 22-36.
- [18] S.H. Mousavi, A.B. Khanikaev, Z. Wang, Topologically protected elastic waves in phononic metamaterials, *Nature Communications* 6(1) (2015) 8682.
- [19] K. Takata, M. Notomi, Photonic Topological Insulating Phase Induced Solely by Gain and Loss, *Physical Review Letters* 121(21) (2018) 213902.
- [20] B. Peng, Ş.K. Özdemir, S. Rotter, H. Yilmaz, M. Liertzer, F. Monifi, C.M. Bender, F. Nori, L. Yang, Loss-induced suppression and revival of lasing, *Science* 346(6207) (2014) 328-332.
- [21] H. Zhao, P. Miao, M.H. Teimourpour, S. Malzard, R. El-Ganainy, H. Schomerus, L. Feng, Topological hybrid silicon microlasers, *Nature Communications* 9(1) (2018) 981.
- [22] D. Liu, Z. Wang, Z. Cheng, H. Hu, Q. Wang, H. Xue, B. Zhang, Y. Luo, Simultaneous Manipulation of Line-Gap and Point-Gap Topologies in Non-Hermitian Lattices, *Laser & Photonics Reviews* 17(4) (2023) 2200371.
- [23] L. Xiao, T. Deng, K. Wang, G. Zhu, Z. Wang, W. Yi, P. Xue, Non-Hermitian bulk–boundary correspondence in quantum dynamics, *Nature Physics* 16(7) (2020) 761-766.
- [24] T.-S. Deng, W. Yi, Non-Bloch topological invariants in a non-Hermitian domain wall system, *Physical Review B* 100(3) (2019) 035102.
- [25] S. Yao, Z. Wang, Edge States and Topological Invariants of Non-Hermitian Systems, *Physical Review Letters* 121(8) (2018) 086803.

- [26] M. Brandenbourger, X. Locsin, E. Lerner, C. Coullais, Non-reciprocal robotic metamaterials, *Nature Communications* 10(1) (2019) 4608.
- [27] C. Luo, Y. Song, C. Zhao, S. Thirumalai, I. Ladner, M.A. Cullinan, J.B. Hopkins, Design and fabrication of a three-dimensional meso-sized robotic metamaterial with actively controlled properties, *Materials Horizons* 7(1) (2020) 229-235.
- [28] S.C. Goldstein, J.D. Campbell, T.C. Mowry, Programmable matter, *Computer* 38(6) (2005) 99-101.
- [29] Y. Song, P.C. Dohm, B. Haghpanah, A. Vaziri, J.B. Hopkins, An Active Microarchitected Material that Utilizes Piezo Actuators to Achieve Programmable Properties *Advanced Engineering Materials* 18(7) (2016) 1113-1117.
- [30] J. Li, Y. Yuan, J. Wang, R. Bao, W. Chen, Propagation of nonlinear waves in graded flexible metamaterials, *International Journal of Impact Engineering* 156 (2021) 103924.
- [31] Q. Zhang, A.V. Cherkasov, C. Xie, N. Arora, S. Rudykh, Nonlinear elastic vector solitons in hard-magnetic soft mechanical metamaterials, *International Journal of Solids and Structures* 280 (2023) 112396.
- [32] B. Deng, P. Wang, Q. He, V. Tournat, K. Bertoldi, Metamaterials with amplitude gaps for elastic solitons, *Nature Communications* 9(1) (2018) 3410.
- [33] S. Liu, R. Shao, S. Ma, L. Zhang, O. You, H. Wu, Y.J. Xiang, T.J. Cui, S. Zhang, Non-Hermitian Skin Effect in a Non-Hermitian Electrical Circuit, *Research* 2021.
- [34] Y. Zhou, Y. Zhang, C.Q. Chen, Amplitude-dependent boundary modes in topological mechanical lattices, *Journal of the Mechanics and Physics of Solids* 153 (2021) 104482.
- [35] C.L. Kane, T.C. Lubensky, Topological boundary modes in isostatic lattices, *Nature Physics* 10(1) (2014) 39-45.

Appendix A: Modeling of the pure displacement framework

To solve the dispersion relation of displacement under PBC, consider the solution of Eq.(1) in the form of Bloch wave, namely, $u_n = \tilde{u}(q)e^{i(qn-ot)}$, and substitute Eq.(1) to get:

$$-m\omega^2 = (k_l - k_n)e^{iq} + (k_l + k_n)e^{-iq} - 2k_l. \quad (\text{A-1})$$

The spectrum of PBC is shown in Fig. A. When $k_n \neq 0$, the branches of the PBC form a loop geometry. For a reference point ω within the closed loop, the point gap can be well defined, and the corresponding point gap has a spectral winding number characteristic, which is expressed as:

$$W(\omega) = \frac{1}{2\pi i} \oint_C \frac{1}{C(q) - \omega} dC(q), \quad (\text{A-2})$$

where, $C(q) = (k_l - k_n)e^{iq} + (k_l + k_n)e^{-iq} - 2k_l$. For static problems, the reference point is $\omega = 0$, When $k_n = 0$, the loop degenerates into a straight line, where $W(0) = 0$, but when $k_n \neq 0$, the integral curve passes through the singularity of the integrand function ($C(0) = 0$), as shown in Fig. A(a) and Fig. A(c), and the integral corresponding to Eq. (A-2) is singular, namely, $W(0)$ cannot characterize the topological properties of $k_n < 0$ and $k_n > 0$.

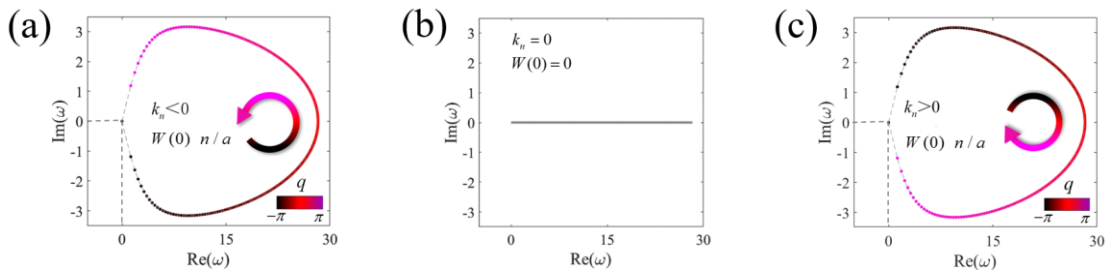


Fig. A Spectra of structures under PBC

OBC can be expressed as the left side exerting a rightward force $F_{0,1} = -k_n(u_0 + u_1)$, and the right side exerting a leftward force $F_{N,N-1} = -k_n(u_{N-1} + u_N)$.

The schematic diagram of finite structure modeling is shown in Fig. 2(a) in section 3.1. The governing equation of the one-dimensional chain is written as:

$$m\ddot{u}_0 = -(k_l + k_n)u_0 + (k_l - k_n)u_1, \quad (\text{A-3-a})$$

$$m\ddot{u}_n = (k_l - k_n)u_{n+1} + (k_l + k_n)u_{n-1} - 2k_l u_n, n \in [1, N-1], \quad (\text{A-3-b})$$

$$m\ddot{u}_N = (k_l + k_n)u_{N-1} - (k_l - k_n)u_N. \quad (\text{A-3-c})$$

Eq. (A.3) can be written in matrix form:

$$-m\omega^2 \mathbf{U} = \mathbf{D}_{N' \times N'} \mathbf{U}, \quad (\text{A-4})$$

where,

$$\mathbf{D}_{N' \times N'} = \begin{bmatrix} -c_1 & c_2 & & \dots & & 0 \\ 0 & c_2 & -(c_1+c_2) & c_1 & \dots & 0 \\ 0 & \dots & c_2 & -(c_1+c_2) & c_1 & \dots & 0 \\ 0 & \dots & & c_2 & -(c_1+c_2) & c_1 & 0 \\ 0 & & & & \dots & c_1 & -c_2 \end{bmatrix}.$$

Eq.(A-4) is numerically solved to obtain the spectrum diagram of the finite structure. In the band gap, an isolated band appears at zero frequency, which is shown in Fig. 2 (b) in section 3.1. According to the analysis in section 3.1, the zero-frequency mode can be reduced to a mode similar to the zero-energy mode, and the governing equation can be reduced to: $F_{n,n+1} = -k_l(u_{n+1} - u_n)$, $n \in [0, N-1]$. Write the above formula in matrix form:

$$\mathbf{C}_{(N'-1) \times N'} \begin{bmatrix} u_0 \\ u_1 \\ \vdots \\ u_{N-1} \\ u_N \end{bmatrix} = \begin{bmatrix} c_1 & -c_2 & \dots & & 0 \\ 0 & c_1 & -c_2 & \dots & 0 \\ 0 & \dots & c_1 & -c_2 & \dots & 0 \\ 0 & \dots & & c_1 & -c_2 & 0 \\ 0 & \dots & & & c_1 & -c_2 \end{bmatrix} \begin{bmatrix} u_0 \\ u_1 \\ \vdots \\ u_{N-1} \\ u_N \end{bmatrix} = 0, \quad (\text{A-5})$$

where, $\mathbf{C}_{(N'-1) \times N'}$ is the compatibility matrix.

In the pure displacement frame, the governing equations of statics are as follows:

$$\text{BC-L: } 0 = k_l(u_1 - u_0) + F_0, 0 = (k_l + k_n)u_{N-1} - (k_l - k_n)u_N, \quad (\text{A-6})$$

$$\text{BC-R: } 0 = -(k_l + k_n)u_0 + (k_l - k_n)u, 0 = k_l(u_N - u_{N-1}) + F_N, \quad (\text{A-7})$$

$$0 = (k_l - k_n)u_{n+1} + (k_l + k_n)u_{n-1} - 2k_l u_n, \quad n \in [1, N-1]. \quad (\text{A-8})$$

Assuming that the envelope of the displacement field has a small gradient, a continuous displacement field $u(X)$ is introduced such that $u_n = u(X_n)$. Perform a Taylor expansion of $u_{n\pm 1} = u(X_n \pm 1)$ at X_n :

$$u_{n\pm 1} \approx u(X_n) \pm \left. \frac{\partial u}{\partial X} \right|_{X=X_n} + \frac{1}{2} \left. \frac{\partial^2 u}{\partial X^2} \right|_{X=X_n}. \quad (\text{A-9})$$

Substitute Eq.(A-9) into Eq.(A-8):

$$\frac{d^2 u}{dX^2} - \frac{1}{\lambda_u^*} \frac{du}{dX} = 0, \quad (\text{A-10})$$

where $\lambda_u^* = k_l / (2k_n)$ is the characteristic decay length of the displacement field distribution under the continuum limit. Eq. (A-10) is a second-order linear differential equation whose solution consists of a linear combination of $\exp(X / \lambda^*)$ and $\exp(-X / \lambda^*)$, namely:

$$u = C_1 e^{X/\lambda^*} + C_2 e^{-X/\lambda^*}, \quad (\text{A-11})$$

where, C_1 and C_2 are integral constants determined by the boundary conditions (Eq. (A-6) or Eq. (A-7)). The results of the continuum model are shown in the red solid line in Fig. 2 (d) of section 3.1.

When the left side is excited, the boundary condition BC-L is selected, and the displacement generated by the 0-th node is $u_0^L = -F_0 / [k_l(g-1)]$. According to the geometric distribution law, $u_N^L = -g^N F_0 / [k_l(g-1)]$. When the right side is excited, the boundary condition BC-R is selected, and finally the 0-th displacement $u_0^R = -g^{-N} F_0 / [k_l(1-g^{-1})]$ is obtained. The output displacement difference between the left excitation and the right excitation is:

$$\Delta u = u_N^L + u_0^R = -\left[\frac{g^N}{k_l(g-1)} + \frac{g^{-N}}{k_l(1-g^{-1})} \right] F_0 = \kappa_u F_0, \quad (\text{A-12})$$

where, κ_u is non-reciprocal susceptibility.

Appendix B: Modeling of eccentric excitation cases

(i) Geometrically linear case

The governing equation of angle is:

$$J \frac{\partial^2 \theta_n}{\partial t^2} = -k_\theta (\theta_{n+1} + \theta_{n-1} + 4\theta_n) + k_s l^2 (\theta_{n+1} + \theta_{n-1} - 2\theta_n). \quad (\text{B-1})$$

Set $\delta\theta_n$ as the Bloch wave solution of the form $\theta_n = \tilde{\theta}(q)e^{i(qn - \omega t)}$, and the dispersion relation of the corner is as follows:

$$-J\omega^2 = -k_\theta (e^{iq} + e^{-iq} + 4) + k_s l^2 (e^{iq} + e^{-iq} - 2), \quad (\text{B-2})$$

k_θ is non-zero, which will result in $\omega(q)|_{q=0}$ never being zero, namely, the band gap is always open.

(ii) Geometric nonlinear case

In the case of left excitation, the governing equation from the 1-th node to the (N-1)-th node is:

$$\begin{aligned} 0 = & -k_\theta (\theta_{n+1} + \theta_{n-1} + 4\theta_n) \\ & -k_l (f_{n-1,n} + f_{n,n+1}) l \sin \theta_n \\ & + k_s (\sin \theta_{n+1} + \sin \theta_{n-1} - 2\sin \theta_n) l^2 \cos \theta_n, \end{aligned} \quad (\text{B-3})$$

where,

$$f_{n,n+1} = k_l [u_{n+1} - u_n + (l + \frac{l_h}{2})(2 - \cos \theta_n - \cos \theta_{n+1})], \quad (\text{B-4})$$

$f_{n,n+1}$ is the tension provided by the shim between the n -th node and the $(n+1)$ -th node.

Substituting Eq. (12) into Eq. (B-4), $f_{n,n+1}$ is reduced to:

$$f_{n,n+1} = k_l u_N (g^{n+1} - g^n), \quad n \in [0, N-1] \quad (\text{B-5})$$

Substituting Eq. (B-5) into Eq. (B-3), after a continuous angle field $\theta(X)$ is introduced such that $\theta_n = \theta(X_n)$, the governing equation of the angle is obtained:

$$\frac{d^2\theta}{dX^2} - \frac{2k_l l u_N g^x \ln g + 6k_\theta}{k_s l^2 - k_\theta} \theta = 0. \quad (\text{B-6})$$

The governing equation for the N -th node can be written as:

$$\begin{aligned} 0 = & -k_\theta(\theta_{N-1} + 3\theta_N) + k_s l^2 (\sin \theta_{N-1} - \sin \theta_N) \\ & - k_l [u_N - u_{N-1} + (l + \frac{l_h}{2})(2 - \cos \theta_N - \cos \theta_{N-1})] l \sin \theta_N. \end{aligned} \quad (\text{B-7})$$

According to Eq. (B-5), the tension provided by the shim between the $(N-1)$ -th node and the N -th node is $f_{N-1,N} = k_l u_N (g^N - g^{N-1})$, and Eq. (B-7) is transformed into:

$$f_{N-1,N} = - \left[\frac{3k_\theta}{l} \frac{\theta(N)}{\sin \theta(N)} + \left(\frac{k_s l^2 - k_\theta}{l} \right) \frac{(d\theta/dX)|_{X=N}}{\sin \theta_N} \right]. \quad (\text{B-8})$$

The angle distribution can only have increasing intervals in two cases, one is that $\theta(N)$ and $(d\theta/dX)|_{X=N}$ are greater than 0 (as shown in Fig. 5(e)), and the other is that $\theta(N)$ and $(d\theta/dX)|_{X=N}$ are less than 0, but the occurrence of these two cases require $f_{N-1,N} < 0$, namely, the force of the shim must be pressure.

Appendix C: Dynamics modeling

The governing equations of the dynamics are as follows:

$$\begin{aligned} m \frac{\partial^2 u_n}{\partial t^2} = & k_n (u_{n-1} - u_{n+1}) + k_l (u_{n+1} + u_{n-1} - 2u_n) \\ & + k_l (l + \frac{l_h}{2})(\cos \theta_{n-1} - \cos \theta_{n+1}), \end{aligned} \quad (\text{C-1})$$

$$\begin{aligned} J \frac{\partial^2 \theta_n}{\partial t^2} = & -k_\theta (\theta_{n+1} + \theta_{n-1} + 4\theta_n) \\ & - k_l (u_{n+1} - u_{n-1}) l \sin \theta_n \\ & - k_l (4 - 2\cos \theta_n - \cos \theta_{n+1} - \cos \theta_{n-1}) (l + \frac{l_h}{2}) l \sin \theta_n \\ & + k_s (\sin \theta_{n+1} + \sin \theta_{n-1} - 2\sin \theta_n) l^2 \cos \theta_n, \end{aligned} \quad (\text{C-2})$$

Eqs.(C-1) and (C-2) are normalized as follows: $U = u/(2l)$, $X = x/(2l)$, $T = t\sqrt{k_l/m}$

$K_\theta = k_\theta/k_l l^2$, $K_s = k_s/k_l$, $K_n = k_n/k_l$, $\alpha^2 = ml^2/J$, $\beta = 1 + l_h/(2l)$. The continuum

models of Eqs.(C-1) and (C-2) is:

$$\frac{\partial^2 U}{\partial T^2} = \frac{\partial^2 U}{\partial X^2} + \beta\theta \frac{\partial \theta}{\partial X} - 2K_n \frac{\partial U}{\partial X}, \quad (\text{C-3})$$

$$\frac{1}{\alpha^2} \frac{\partial^2 \theta}{\partial T^2} = -K_\theta \left(6\theta + \frac{\partial^2 \theta}{\partial X^2}\right) + K_s \frac{\partial^2 \theta}{\partial X^2} - 2\left[2 \frac{\partial U}{\partial X} + \beta\theta^2\right]\theta. \quad (\text{C-4})$$

In the case of $K_n = 0$, the soliton solution corresponding to Eqs. (C-3) and (C-4)

is:

$$\theta = A_p \operatorname{sech} \frac{X - cT}{W_p}, \quad (\text{C-5})$$

$$U = \frac{3K_\theta W_p}{c^2} \left(1 - \tanh \frac{X - cT}{W_p}\right), \quad (\text{C-6})$$

where,

$$A_p = \sqrt{\frac{6K_\theta(1-c^2)}{\beta c^2}} \quad (\text{C-7})$$

is the amplitude of the pulse soliton,

$$W_p = \sqrt{\frac{K_s - K_\theta - c^2 / \alpha^2}{6K_\theta}} \quad (\text{C-8})$$

is the width of the pulse soliton, and c is the wave speed. The soliton solution requires that W_p must be real, namely, $c^2 < \alpha^2(K_s - K_\theta)$, which means that Eq. (C-7) has a minimum value:

$$A_p > \sqrt{\frac{6K_\theta}{\beta} \left[\frac{1}{\alpha^2(K_s - K_\theta)} - 1 \right]} = A_p^{\text{gap}}, \quad (\text{C-9})$$

where, A_p^{gap} is the amplitude gap.

The total energy for the n -th pair of crosses can be expressed as:

$$e_n = m \left(\frac{\partial u_n}{\partial t} \right)^2 + J \left(\frac{\partial \theta_n}{\partial t} \right)^2 + k_\theta (\theta_n + \theta_{n+1})^2 + \frac{1}{2} k_\theta (2\theta_n)^2 + k_s l^2 (\sin \theta_{n+1} - \sin \theta_n)^2 + k_l (u_{n+1} - u_n + 2l - l \cos \theta_n - l \cos \theta_{n+1})^2, \quad (\text{C-10})$$

Eqs. (C-5) and (C-6) are substituted into Eq. (C-10) to obtain the energy carried by the soliton:

$$\begin{aligned}
E(c) &= \int_{-\infty}^{+\infty} e(X) dX = \frac{4}{3}W[k_l l^2 \frac{36K_\theta^2}{c^2} + 36k_l^2 K_\theta^2] \\
&+ \frac{2}{3}W[k_l l^2 \frac{36K_\theta^2(1-c^2)}{\alpha^2(K_s - K_\theta - c^2/\alpha^2)} + k_s l^2 \frac{36K_\theta^2(1-c^2)}{c^2(K_s - K_\theta - c^2/\alpha^2)}] \quad (C-11) \\
&+ \frac{2}{3}Wk_\theta \frac{36K_\theta(1-c^2)}{c^2}.
\end{aligned}$$

The relationship between $A_p(c)$ and $E(c)$ is shown in Fig. C.

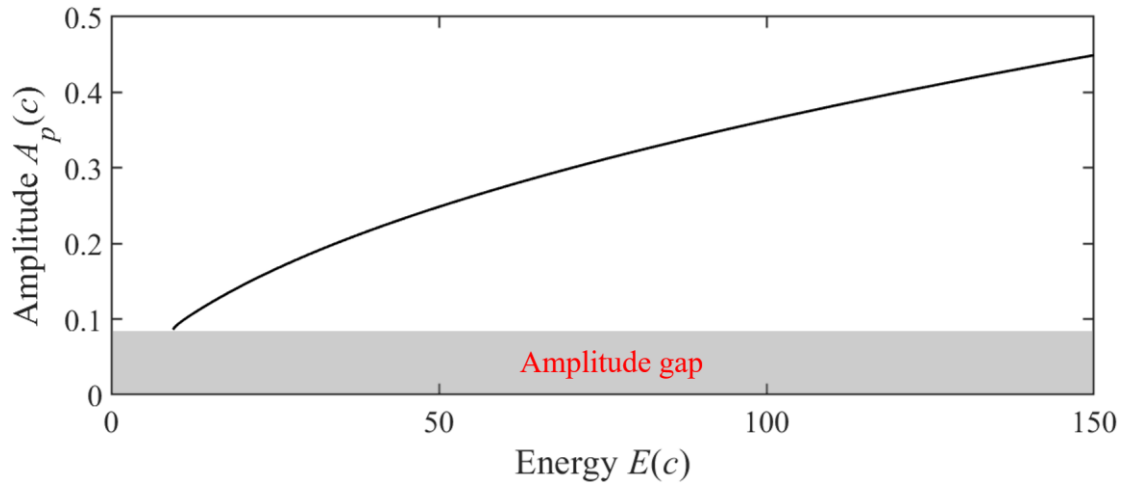


Fig. C Diagram of the relationship between energy and amplitude